March 2007

# Surface properties of $LiCoO_2$, $LiNiO_2$ and $LiNi_{1-x}Co_xO_2$

Anthony W. Moses
*University of Nebraska - Lincoln*

Harry G. Garcia Flores,
*University of Nebraska - Lincoln*

Jong-Gyu Kim
*University of Nebraska - Lincoln*, jkim3@unl.edu

Marjorie Langell
*University of Nebraska - Lincoln*, mlangell1@unl.edu

Published in *Applied Surface Science* 253:10 (March 15, 2007), pp. 4782–4791. doi:10.1016/j.apsusc.2006.10.044  http://www.sciencedirect.com/science/journal/01694332

Submitted June 23, 2006; accepted October 22, 2006; published online November 29, 2006.

# Surface properties of $LiCoO_2$, $LiNiO_2$ and $LiNi_{1-x}Co_xO_2$

Anthony W. Moses, Harry G. Garcia Flores, Jong-Gyu Kim, and Marjorie A. Langell

*Department of Chemistry, University of Nebraska–Lincoln, Lincoln, Nebraska 68588-0304*

**Abstract:** The surface composition and chemical environment of $LiCoO_2$, hexagonal $LiNiO_2$, cubic $LiNiO_2$, and the mixed transition metal oxide $LiNi_{0.5}Co_{0.5}O_2$ have been determined by Auger electron and X-ray photoelectron spectroscopies. While the $LiCoO_2$ surface properties can easily be extrapolated from bulk composition, the nickel-containing materials are less straightforward. Their surface concentration tends to be depleted in lithium relative to that of the bulk and shows an atypical chemical environment for the constituent elements. The Ni 2p XPS photoemission suggests a near " NiO-like" selvedge through the XPS binding energies and satellite structure which are essentially identical to that of NiO; the spectrum appears fairly insensitive to lithium concentration. Although there is little evidence for higher binding energy $Ni^{3+}$ species or for an electron poor $Ni^{2.\delta+}$-derived band structure in the XPS, the lattice oxygen is very electron-rich and yields among the lowest binding energies reported for a transition metal oxide. The nickel-containing lithium oxide selvedge is thus not simply "NiO" and the surface lithium cations have a measurable effect on the electronic structure even in their more highly depleted levels. This is explained in the context of the charge-transfer model of the oxide band structure.

**Keywords:** Lithium cobalt oxide; Lithium nickel oxide; XPS

## 1. Introduction

Rechargeable lithium batteries are widely used in portable electronic devices, such as cell phones and computer notebooks, and their usage promises to increase even further as new applications for them develop [1], [2], [3] and [4]. Both the lightest of all metals and the one with the highest standard reduction potential [5], lithium promises high energy density when used as the anode material in rechargeable battery architecture. Lithium batteries can typically be made small-sized, are low-maintenance and can be made to function without memory effects or the requirement for scheduled cycling to prolong battery life.

Because of safety considerations, commercial lithium ion batteries employ solid state lithium oxide compounds as the source of lithium ion. Lithium cobalt oxide is one of the earliest, and in many ways most successful, anode materials used for this purpose. Batteries employing $LiCoO_2$ anodes are still among the highest energy density lithium batteries available (~140 Wh/kg [6]), show powder densities as high as 5500 W/kg [7], can be used over a reasonably large temperature range of ~ −10 to 100 °C [8] and [9] and have the longest life expectancy of presently available materials. $LiCoO_2$ does, however, suffer from relatively high cost [10] and environmental processing and disposal problems [11]. For this reason, the related materials $LiNiO_2$ and $LiNi_{1-x}Co_xO_2$ have been studied as potential substitutes for the lithium ion anode [12], [13], [14], [15], [16], [17] and [18].

$LiCoO_2$ and "hexagonal" $LiNiO_2$ can be idealized as cubic (rocksalt) structures in which planes of the much smaller lithium ions alternate with cobalt or nickel ions along the $\langle 1\,1\,1 \rangle$ direction (Fig. 1) lowering the symmetry to the rhombohedral $R\bar{3}m$ [19], [20] and [21]. Even in its most fully lithium-charged state, the lithium nickel oxide is difficult to obtain stoichiometrically and its composition is more accurately represented as $Li_{1-z}Ni_{1+z}O_2$ where lithium vacancies are compensated by excess nickel located within the lithium layer [20] and [21]. Lithium ion conduction occurs along the lithium-occupied (1 1 1) planes, and good cycling characteristics of the battery depend upon repeated lithium depopulation and repop-

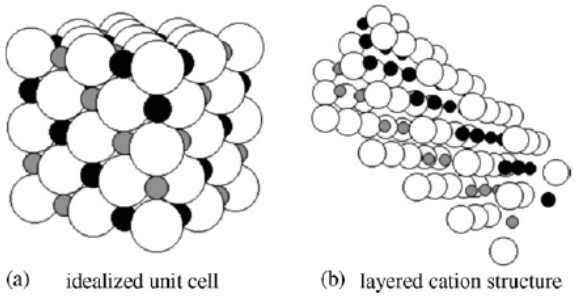


Fig. 1. $LiMO_2$ structure for (a) the idealized unit cell close packed in oxygen (white) with alternating lithium (grey) and transition metal (black) planes, and (b) a view along the (1 1 1) planes emphasizing the cation layers.

ulation of the sites with minimum cumulative damage to the structure. Cubic $LiNiO_2$ ($Fm\bar{3}m$) can also be synthesized, although the bulk tends to be vacancy-laden. A phase transition from hexagonal to the cubic form of $LiNiO_2$ has been reported at about 720 °C in air, a process which is slowed and shifts to higher temperatures under flowing $O_2$ or other oxidizing conditions.

While $LiNiO_2$ has a higher specific capacity than $LiCoO_2$, nickel occupation of lithium lattice sites interferes with lithium ion mobility [22]. $LiNiO_2$ is also thermally and electrochemically less stable than $LiCoO_2$, showing loss of oxygen, irreversible delithiation, a variety of phase transition problems and cycling-induced microcrack formation upon charging to voltages higher than 4.2 V [16]. The mixed-metal $LiNi_{1-x}Co_xO_2$ has been proposed as a compromise to improve upon this situation by substituting some but not all of the cobalt with nickel. Bulk $LiNi_{1-x}Co_xO_2$ shows random nickel/cobalt site occupancy based on the relative stoichiometry of the transition metals in the bulk compound [13] and [15].

From a more fundamental viewpoint, the materials raise interesting questions about the nature of the transition metal cation in the solid state. Formal oxidation states for $LiCoO_2$ are straightforward. Assigning formal charges of $Li^+$ and $O^{2-}$ yields a nominal oxidation state of $Co^{3+}$ in which the $3d^6$ cation adopts a very stable, low-spin diamagnetic state with a full $t_{2g}$ subshell. Following the same reasoning for $LiNiO_2$, however, requires the formation of $Ni^{3+}$, an uncommon state for solid state nickel oxides and one that is often stabilized by the formation of defects or hydroxides that produce mixed $Ni^{2+}/Ni^{3+}$ oxidation states. Indeed, two general descriptions have emerged in the literature in relation to the chemical nature of nickel in $LiNiO_2$, one analogous to that found for $LiCoO_2$ in which the oxidation state for the nickel is $Ni^{3+}$[23], [24], [25], [26], [27] and [28] and a second one that relies on localized $Ni^{2+}$-$O^-$ pairs in which charge is transferred from a neighboring lattice oxygen onto the nickel to preserve, or at least more closely approximate, the favored $2^+$ state [29], [30], [31], [32], [33] and [34]. We present here a study of surface composition of $LiCoO_2$, $LiNiO_2$ and $LiNi_{0.5}Co_{0.5}O_2$ which suggests that, at least in the near-surface region, the nickel-containing lithium metal oxide is stabilized by dilithiation to produce a nickel cation with an average electron density closer to that of the more favored $Ni^{2+}$ state. However, these materials are not simply equivalent to "NiO" and retain an extremely electron-rich lattice oxygen species even for substrates that retain 50% or more of the stoichiometric lithium concentration in the near-surface region.

## 2. Experimental

Lithium cobalt(III) oxide (99%) was obtained from Aldrich and used without further bulk purification. Its integrity was verified by powder X-ray diffraction (XRD), performed with a Rigaku D-Max/B Horizontal Q/2Q X-ray diffractometer using Cu Kα radiation. The powder was ground with a mortar and pestle to present a fresh surface prior to introduction to the ultrahigh vacuum (UHV) chamber for surface analysis.

Hexagonal ($R\bar{3}m$) and cubic ($Fm\bar{3}m$) $LiNiO_2$ powdered samples were synthesized by sol–gel methods [35], [36] and [37]. LiOH (Aldrich, 98%) and $NH_4OH$ (Fisher, 29%) were co-dissolved in distilled water and to this an aqueous solution of nickel nitrate ($Ni(NO_3)_2{\cdot}6H_2O$, Aldrich, 98%) was added, turning the colorless solution light blue. Excess water and ammonia were removed at room temperature by use of a roto-evaporator. The resulting gel was transferred to a ceramic boat with the aid of liquid nitrogen and heated at 90 °C to dry the sample completely. The resulting black powder was heated under a stream of gently flowing oxygen for 24 h at 600 °C to produce hexagonal $LiNiO_2$ (hexagonal I) and, additionally, under air for 5 h at 780 °C to produce the cubic sample. Ethanol-based sol–gel synthesis was also used to produce hexagonal $LiNiO_2$ (hexagonal II) in which the nickel from the nickel nitrate was chelated with citric acid (Research Chemicals, Ltd. 99+%). The sol–gel was roto-evaporated to dryness, precalcinated at 450 °C under air for 12 h and heated under gently flowing $O_2$ at 750 °C for 24 h [38]. X-ray diffraction (XRD) confirmed the integrity of the samples and differences in surface composition for the two sol–gel preparations of the hexagonal $LiNiO_2$ are discussed below.

$LiNi_{0.5}Co_{0.5}O_2$ samples were also synthesized by sol–gel methods [39] and [40]. $Li(CH_3CO_2)_2{\cdot}4H_2O$, $Ni(CH_3CO_2)_2{\cdot}4H_2O$ and $Co(CH_3CO_2)_2{\cdot}4H_2O$ (Aldrich, 98%) in appropriate stoichiometry were co-dissolved in distilled water. Citric acid was then added to the metal acetate solution, and excess water was evaporated at 90 °C on a hot plate, resulting in a dark purple gel. The gel was transferred to a ceramic boat and heated at 700 °C for periods between 6 and 36 h in air. Samples that produced the best quality XRD formed after approximately 24 h heating under these conditions and are the $LiNi_{0.5}Co_{0.5}O_2$ samples presented here for surface analysis.

Surface analysis was performed in a 40 L stainless steel bell jar with a typical base pressure of $4 \times 10^{-8}$ Pa. The bell jar was equipped with a rapid transfer load-lock obviating the need to bake out the chamber following sample transfer. The powder samples were freshly ground prior to surface analysis and mounted by pressing into either indium foil or gold mesh. When mounted on gold mesh, the sample mount permitted controllable heating to temperatures of up to approximately 800 °C under UHV and provided a reference in X-ray photoelectron spectroscopy (XPS) through the Au $4f_{7/2}$ transi-

tion at 84.0 eV. However, the gold foil interfered with lithium analysis in both Auger electron spectroscopy (AES) and XPS due to overlap between lithium and gold transitions. Indium provided better adhesion, allowing thicker lithium oxide samples, and thus minimal interference from indium in the spectra, but could not be used above room temperature. Provisions were available for argon ion bombardment with either sample mount.

AES and XPS were obtained with a Physical Electronics 15-255 G double pass cylindrical mirror analyzer. AES was taken at 2 and 3 KeV primary beam energies as differential spectra in a lock-in mode with 2 eV modulation energy and a scan rate of 1 eV/s. XP spectra were obtained with Mg Kα radiation (1253.6 eV) in constant pass energy mode in 0.1 eV step increments and 50 ms dwell time per step. Unless otherwise noted in the figure caption, pass energies of 50 eV were employed. Binding energies were calibrated relative to adventitious carbon at 284.6 eV and/or to the main Au $4f_{7/2}$ peak, taken as 84.0 eV, depending upon the sample mount and surface cleanliness. For samples with both gold and adventitious carbon signals, the calibrated binding energies obtained with the two different references were equal to within the precision of the technique, approximately 0.2 eV.

## 3. Results

Powder X-ray diffraction (XRD) data are shown in Fig. 2 for representative samples of the lithium metal oxide samples, with Miller indices of the more intense features labeled above the $LiCoO_2$ trace. The XRD data are characteristic of the materials, although the $LiNi_{0.5}Co_{0.5}O_2$ trace appears broader than that of the other samples even after extensive efforts were made to optimize synthesis conditions for this mixed transition metal oxide. Similar quality XRD are found for $LiNi_{0.5}Co_{0.5}O_2$ powders elsewhere in the literature [13], [40] and [41], indicating that it is difficult to form a truly homogenous solid solution in which nickel and cobalt are randomly distributed within the (1 1 1) transition metal planes. Not surprisingly, unit cell dimensions increase with increasing nickel content for the hexagonal samples, which is evident through a decrease in $2\theta$ for diffraction from a particular lattice plane.

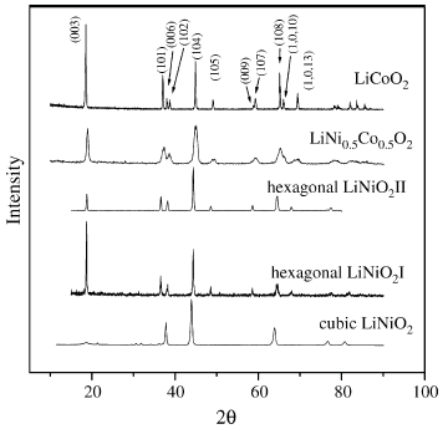


Fig. 2. X-ray diffraction data for a representative sample of $LiCoO_2$, $LiNi_{0.5}Co_{0.5}O_2$, hexagonal $LiNiO_2$ and cubic $LiNiO_2$. Miller indices for the hexagonal ($R\bar{3}m$) samples are indicated above the $LiCoO_2$ trace.

Additionally, the nickel-containing samples show considerable variability in relative intensity of their XRD diffraction features, particularly those related to (00N)/(10N) lattice planes, indicating that nickel content and synthesis conditions affect the order of the crystal structure. For hexagonal $LiNiO_2$, the intensity ratio of the two most prominent features in these series, I(0 0 3)/I(1 0 4), has previously been demonstrated to correlate with lithium and transition metal ordering in forming the alternating Li/transition metal (1 1 1) planes and I(0 0 3)/I(1 0 4) ratios of 1.5 or above have generally taken to be a sign of good bulk lithium order [38]. Two samples of the hexagonal lithium nickel oxide, $LiNiO_2$ I and $LiNiO_2$ II, synthesized by the slightly different sol–gel methods described in the Section 2, are reported here with I(0 0 3)/I(1 0 4) = 0.40 and 1.6, respectively. In comparison, the $LiCoO_2$ (0 0 3)/(1 0 4) intensity ratio for the data in Fig. 2 is 1.8.

Cubic $LiNiO_2$ $Fm\bar{3}m$ is found as a high-temperature form of the hexagonal sample with a phase transition at 720 °C in air that is only partially reversible [42]. Its formation can be suppressed [43] when the hexagonal form is desired by increasing the oxygen flow rate during the high-temperature stage of its synthesis. Cubic $LiNiO_2$ has been reported to have a relatively high concentration of oxygen vacancy defects when compared to the hexagonal form [38] and [44]. However, it is also associated with lithium deintercalation, substitution of nickel for lithium within the (1 1 1) lithium planes, and generally poor electrode characteristics. The XRD of Fig. 2 shows the cubic $LiNiO_2$ synthesized by the present methods to be well-ordered in the bulk material, with narrow diffraction features and absence of other crystalline phases, but with a very small I(0 0 3)/I(1 0 4) ratio, as expected for the high-temperature cubic phase known to show significant variability in its lithium nickel site substitution.

The surface of the as-introduced samples is surprisingly clean, given the minimal surface cleaning and pretreatment used in the present set of studies, as can be seen from the representative Auger spectra (AES) of Fig. 3 for hexagonal $LiNiO_2$ (sample I) and the $LiCoO_2$. The very small indium signal found in the AES comes from the foil mounting and is not a contaminant of the lithium metal oxides, themselves. No indium was found on samples from the same synthesis lot mounted on gold foil instead of indium. The cleanliness indicated by the Auger spectra is somewhat deceptive, in that the Auger excitation beam causes severe electron stimulated desorption (ESD) of surface carbonates. When $Li_2CO_3$ powders were placed in the UHV chamber in attempts to acquire reference spectra, ESD was so severe that large pressure bursts were observed immediately upon exposure to the electron beam and no usable spectra could be obtained. X-ray photoemission (XPS) from C 1s and O 1s spectral regions showed carbonate to be detectable by XPS for some, although not all, of the samples studied, as will be described in detail below.

Fig. 4 compares the Co 2p XP spectral region for $LiCoO_2$ and $LiNi_{0.5}Co_{0.5}O_2$, along that of two related oxides, CoO and $Co_3O_4$. The latter two spectra serve for calibration pur-

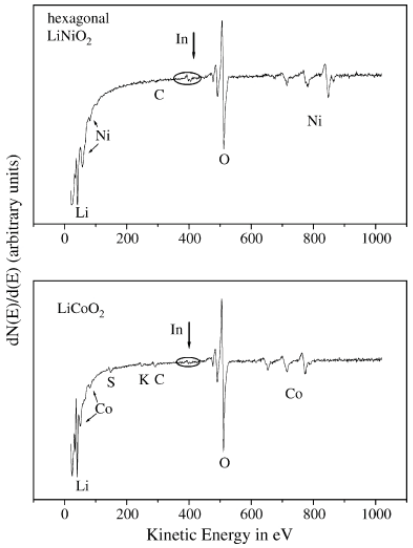


Fig. 3. Auger spectra taken at 2 KeV for representative hexagonal $LiNiO_2$ (sample I) and $LiCoO_2$ samples. These data show impurities to be at the submonolayer level. The samples are mounted on indium foil, which gives rise to a very small indium peak in each spectrum.

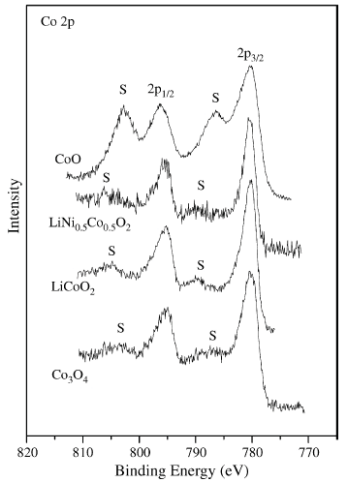


Fig. 4. Cobalt 2p XPS data for $LiNi_{0.5}Co_{0.5}O_2$ and $LiCoO_2$, and for the reference spectra from CoO and $Co_3O_4$. Note that only CoO contains octahedral $Co^{2+}$ and, thus, exhibits the characteristically intense satellite structure. The remaining samples have $Co^{3+}$ occupying octahedral sites. While $Co_3O_4$ also contains $Co^{2+}$, the divalent cation occupies tetrahedral sites in the spinel lattice. Data are taken with a Mg Kα source at 50 eV pass energy.

poses and have been obtained on well-defined single crystal substrates [45], [46] and [47]. The Co 2p spectra of the lithium-containing oxides are characteristic of $Co^{3+}$ in an octahedral or near-octahedral environment, as is also observed for the spinel $Co_3O_4$ structure. In particular, the sharp peak shape of the main $2p_{3/2}$ and $2p_{1/2}$ photoemission is characteristic of a low-spin $d^6$ cation with full, totally spin-paired $t_{2g}$ and empty $e_g$ levels. Because of the enhanced stability of this diamagnetic ion, any shake-up mechanisms that place electron density onto the $Co^{3+}$ cation is suppressed and the satellite structure (marked with "S" in Fig. 4) is very weak. The observed chemical environment of the cobalt cation is reasonable from a charge-balance perspective, in which oxygen is formally $O^{2-}$ balanced by equivalent amounts of $Li^+$ and $Co^{3+}$ in the $LiCoO_2$ lattice.

In contrast, the high-spin $Co^{2+}$ of the CoO lattice allows for significant charge-transfer character between the cobalt $3d^7$ band structure with that of the neighboring lattice oxygen. This valence band character leads to different final state pathways in core-level cobalt photoemission, and is typically represented [48] and [49]:

$$2p^6 3d^7 + h\nu \rightarrow 2p^5 3d^7 + e^- \quad (1a)$$

$$2p^6 3d^7 + h\nu \rightarrow 2p^5 3d^8 L + e^- \quad (1b)$$

where L represents a hole in the oxygen 2p valence band. The $2p^5 3d^8 L$ final state is generally assigned to the lower binding energy main $2p_{3/2}$ and $2p_{1/2}$ spectral features and the satellite structure is associated with the $2p^5 3d^7$ state. Additionally, the main $2p_{3/2}$ and $2p_{1/2}$ transitions in CoO are significantly broader than are those from cobalt-containing spinels, e.g. $Co_3O_4$. This is not an indication of additional cobalt oxidation states in the very well defined CoO(1 0 0) single crystal surface, but instead results from closely lying final states with different charge transfer and d–d coupling effects. In the cobalt lithium oxides, any $Co^{2+}$ present at the surface is below the level of detection for XPS, estimated here at about 10–15% resulting primarily from limitations in the curve-fitting technique. The low-spin $d^6$ nature of the $LiCoO_2$ lattice is not significantly perturbed by the hexagonal distortion introduced by the alternating Li-O and Co-O (1 1 1) sets of planes, and

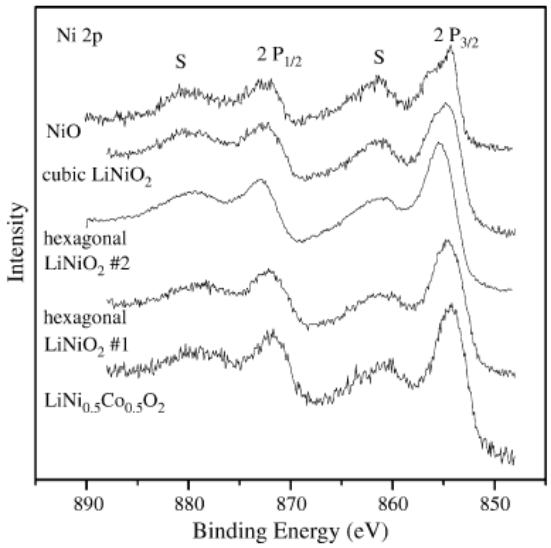


Fig. 5. Ni 2p XPS data for cubic $LiNiO_2$, hexagonal $LiNiO_2$ and $LiNi_{0.5}Co_{0.5}O_2$, and for the reference spectrum from NiO. All spectra are very similar and exhibit intense satellite structure. Data are taken with a Mg Kα source at 50 eV pass energy.

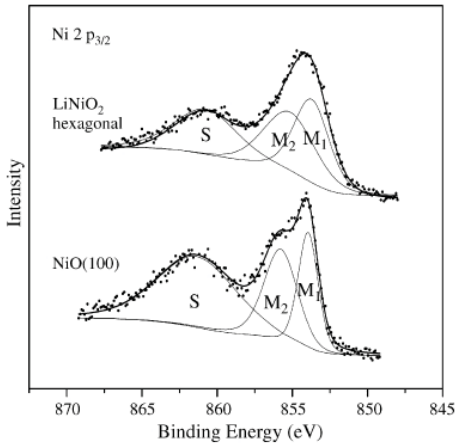


Fig. 6. Peak fit for NiO (1 0 0) and hexagonal $LiNiO_2$ (sample 1) $2p_{3/2}$ XPS. The $LiNiO_2$ spectrum was taken at 50 eV pass energy on a powder sample and the NiO (1 0 0) on a well-defined single crystal at 25 eV pass energy. For both spectra, the main peak fits well with two components at 853.6 and 855.5 eV in approximately 1:1 intensity ratio. For data taken with a 50 eV pass energy the average FWHM is 2.4 and 3.3 eV, respectively.

this effect carries over into the Co 2p spectrum of the mixed-metal oxide $LiNi_{0.5}Co_{0.5}O_2$.

The Ni 2p XP spectra (Fig. 5) provide another example of the charge-transfer nature of an octahedral 2+ cation, this time for $Ni^{2+}$ in NiO as well as for the nickel-containing lithium transition metal oxide samples. Octahedrally-coordinated $Ni^{2+}$ in NiO (1 0 0) shows the same intense satellite structure as CoO and still has very broad features, although there is a somewhat better resolved second "peak" in the main Ni $2p_{3/2}$ core level photoemission than in that of the Co $2p_{3/2}$ spectrum in CoO. Analysis of the 2p region for late 3d transition metal oxides by common peak fitting is not straightforward because significant broadening and multiple final state effects are typically observed for these strongly electron correlated systems.

Although standard curve-fitting procedures might suggest the main component of the Ni $2p_{3/2}$ spectrum of $LiNiO_2$ and $LiNi_{0.5}Co_{0.5}O_2$ samples is best represented by two or more peaks, and thus two or more nickel oxidation states, this broad asymmetric "multiple-peak" structure is identical to that found for NiO. That the peak structure is intrinsic to the single octahedrally-coordinated $Ni^{2+}$ cation can readily be seen from comparison of the NiO (1 0 0) $2p_{3/2}$ spectrum to that of hexagonal $LiNiO_2$ in Fig. 6. Ni 2p peak shapes for the remaining nickel-containing samples were comparable.

XPS from the remaining two components, lithium and oxygen, are potentially informative of the surface chemical composition but can also be more easily misinterpreted in their quantitative aspects. The lithium 1s photoemission peak (Fig. 7) suffers from a low cross section and overlap with cobalt 3p at 60.2 eV and, for samples mounted on gold foil, with the Au $5p_{3/2}$ at approximately 54 eV. The Li 1s binding energy for these materials is quite low compared to other $Li^+$ compounds and is found in the range of 53.3–53.9 eV (Table 1). Each reported binding energy in Table 1 represents the average of ten or more measurements on samples from several different synthesis lots for each material. The value for hexagonal $LiNiO_2$ at 53.3–53.6 eV compares favorably to that previously reported for this material [50] although few other lithium compounds have literature binding energies of this low a value. A second peak is sometimes found at 56.3 eV from surface carbonates (Fig. 7b), a common impurity at the surface of air exposed $LiMO_2$ materials, resulting from the adsorption of $CO_2$ from the ambient [51] either upon storage or during the synthesis process:

$$O_{lattice} + CO_{2(g)} \rightarrow O_{lattice}\text{-}CO_{2(ads)} \rightarrow CO_3^{2-}{}_{surface}$$

as well as from incomplete hydrocarbon combustion in the sol–gel process. It was not possible to obtain hexagonal $LiNiO_2$ from synthesis preparation II (ethanol solvent-based) without at least some carbonate contamination. Small carbonate peaks may also be present in $LiCoO_2$ and $LiNi_{0.5}Co_{0.5}O_2$ spectra in data shown in Fig. 7. However, they are at small enough concentrations as to be obscured by overlap with the Co 3p feature.

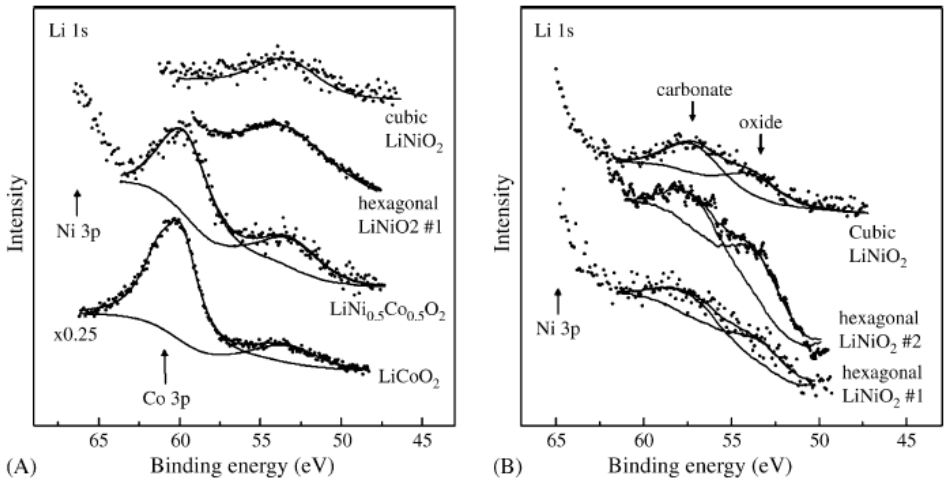


Fig. 7. Lithium XPS for (a) $LiCoO_2$, $LiNi_{0.5}Co_{0.5}O_2$ hexagonal $LiNiO_2$ I and cubic $LiNiO_2$, and (b) hexagonal $LiNiO_2$ I, hexagonal $LiNiO_2$ II and cubic $LiNiO_2$ contaminated at the surface with lithium carbonate. The spectra are taken with Mg Kα radiation at a pass energy of 50 eV.

Table 1
XPS binding energies in eV

| | Li 1s | O 1s | Co $2p_{3/2}$ main satellite | Co $2p_{1/2}$ main satellite | Ni $2p_{3/2}$ main satellite | Ni $2p_{1/2}$ main satellite |
|---|---|---|---|---|---|---|
| $LiCoO_2$ | 53.3 | 529.2 | 779.6<br>788.2 | 794.5<br>804.5 | – | – |
| $LiNiO_2$ (hexagonal I) | 53.3 | 528.4 | – | – | 854.5<br>860.7 | 872.2<br>878.9 |
| $LiNiO_2$ (hexagonal II) | 53.6 | 528.5 | – | – | 854.7<br>860.4 | 872.4<br>878.8 |
| $LiNiO_2$ (cubic) | 53.9 | 528.7 | – | – | 854.5<br>860.9 | 872.1<br>878.7 |
| $Li_{0.5}Co_{0.5}Ni_{0.5}O_2$ | 53.4 | 528.5 | 779.4<br>788.4 | 794.6<br>804.4 | 854.7<br>861.1 | 872.4<br>879.1 |

Representative O 1s and C 1s spectra are shown in Fig. 8 for one set of data from $LiCoO_2$. The O 1s spectral region is highly variable in both peak shape and intensity, and depends strongly upon the history of the sample. There is as much variation within a series of measurements made on a single given compound, but from different synthesis lots or stored for different amounts of time, as there is among the various compounds studied here. However, all O 1s spectra can be described by a fit to varying amounts of four components, three of which are illustrated for the $LiCoO_2$ sample, and the fourth of which occurs only for $LiNi_{0.5}Co_{0.5}O_2$ as is illustrated in Fig. 9. The O 1s carbonate peak observed on some, but not all, samples yields a peak with a binding energy of 532.5 eV and is always matched by a corresponding peak in the C 1s region at 288.2 eV in the proper intensity ratio to the O 1s feature for $CO_3^{2-}$ stoichiometry when appropriate cross sections for photoemission and analyzer transmission function are taken into account [52].

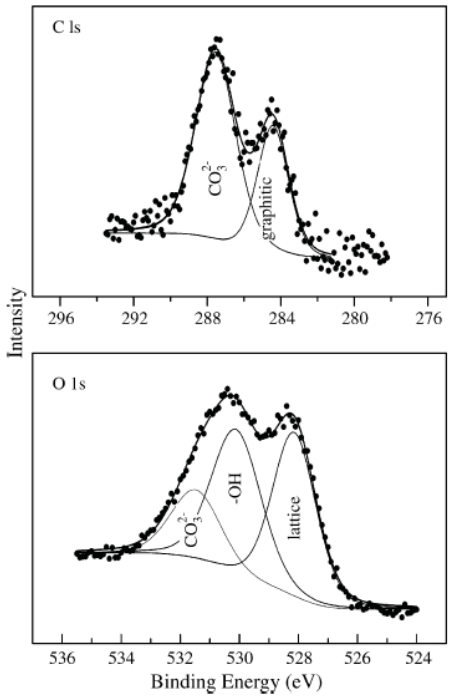


Fig. 8. C 1s and O 1s XPS data for $LiCoO_2$ at 50 eV pass energy. This sample shows both carbonate and hydroxyl contaminants, along with a small amount of adventitious carbon.

The remaining two peaks in Fig. 8 were found on all samples measured in the present set of studies. The lowest binding energy feature, at 528.4–529.2 eV (Table 1), corresponds to the lattice oxygen. At 529.2 eV, the value for the $LiCoO_2$ sample is equal to or only slightly lower than that reported for lattice oxygen in $Co_3O_4$ (529.2–529.5 eV; refs. [53], [54], [55] and [56]), and slightly lower than that for CoO (529.4–529.6 eV; refs. [53], [55], [56], [57] and [58]). Furthermore, doping cobalt oxide powders with lithium for up to 50% of the total metal concentration does not appear to change the O 1s binding energy significantly [54]. The nickel-containing lithium metal oxides are very low in binding energy, however. Their O 1s binding energies are found approximately 1 eV below that of NiO (529.4–529.6 eV; refs. [58], [59], [60] and [61]) and other binary transition metal oxides [52].

Nickel does not have an extended-phase, stable binary spinel oxide for comparison with these data and the $Ni^{3+}$ state is not common in the solid state. Mixed-metal spinels, for example $NiCo_2O_3$, tend to have $Ni^{2+}$cations in octahedral sites and the other cation ($Co^{3+}$) in the 3+ oxidation state in an in

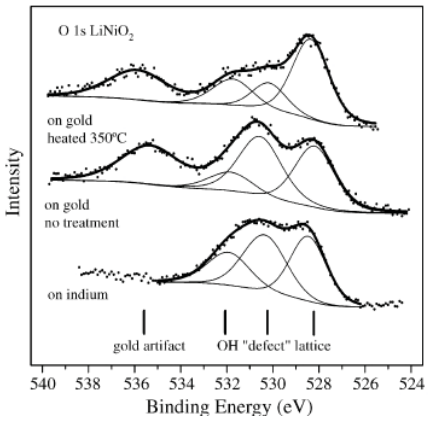


Fig. 9. O 1s XPS data for $LiNi_{0.5}Co_{0.5}O_2$ showing defect oxygen species at 530.5 eV. This peak could be reduced in intensity by annealing the sample under UHV, as is shown after heating at 350 °C for 30 min in the upper trace. There was no detectable carbonate on this sample. The sample holder used with the gold foil support, needed for sample heating, produced an artifact in the O 1s spectrum at high binding energies that was not observed on the indium foil mounting.

verse spinel distribution. For these materials, the O 1s is comparable with that of NiO [62] and [63]. $Ni^{3+}$ has been reported as a "defect structure" in NiO and oxidized nickel metal substrates [64], [65], [66], [67] and [68]; however the O 1s binding energy associated with this species is generally reported at values well in excess of 530 eV. Indeed, there are very few transition metal oxides that have reported lattice oxygen O 1s binding energies at such low binding energy values [52] and the lattice oxygen in the lithium metal oxides is a very electron-rich species.

The remaining feature in Fig. 8 is due to surface hydroxyls (531.4 eV) and was present to some extent on all samples measured in this study. Hydroxylation is also an ubiquitous phenomenon at oxide surfaces and results from interaction with water [53]:

$$\text{M-O}_{\text{lattice}} + \text{H}_2\text{O}_{(g)} \rightarrow \text{O}_{\text{lattice}}\text{-H}_{(ads)} + \text{M-OH}_{(ads)}$$

Prolonged heating of several hours under ultrahigh vacuum at 350 °C reduced, but did not eliminate, the hydroxyl feature and after about 4 h under these conditions the hydroxyl feature was still present at approximately 1/3 monolayer surface coverage.

Both AES and XPS can be used to obtain quantitative information. Because the powdered surfaces are not well-defined structurally, it is assumed that the concentration of species detected within the sampling depth of the technique is uniform over this region and that the relative concentration ratio of two species found at the sample surface is given by [52]:

$$\frac{C_i}{C_j} = \frac{I_i/S_i}{I_j/S_j} \quad (2)$$

Here, $C_i$ is the atomic concentration of the $i$th species, $I_i$ is the spectral intensity of the measured XPS or AES transition used to determine the concentration and $S_i$ is a sensitivity factor for the particular XPS or AES transition. The sensitivity factor includes XPS or AES cross sections, electron escape depth and a spectrometer transmission function for data taken under the specific spectral conditions. These values have been reported elsewhere for nickel and cobalt oxide standard compounds [62] and [63].

Lithium to oxygen sensitivity ratios ($S_{Li}/S_O$) were obtained by calibration with data acquired on a powdered $LiNO_3$ (lithium nitrate) standard sample. For XPS data, $S_{Li}/S_O = 0.056$ for the 1s transitions of lithium and oxygen. For AES data using the lithium 40 eV and the oxygen 510 eV $KL_2L_2$ Auger transitions, $S_{Li}/S_O = 8.3$ at 2 kV Auger excitation beam energy and 5.1 at 3 kV, when data were acquired in the $\partial N(E)/\partial E$ versus $E$ (differentiated) mode. When intensity values were obtained by integrating AES peaks acquired in the $N(E)$ versus $E$ mode, $S_{Li}/S_O = 0.63$ at 2 kV and 0.25 at 3 kV, respectively. Table 2 summarizes the surface concentrations obtained on the lithium metal oxide samples.

The data of Table 2 represent averages made over 10 or more measurements on each compound, including samples from different synthesis lots. Because of simplifying assumptions made in Eq. (2), including that of a homogeneous concentration profile with depth into the surface, the concentration values of Table 2 are most likely not as accurate as the precision of the technique implies. In addition, systematic errors in applying averaged sensitivity factors to specific compounds have been reported to be as high as 20% [52]. However, the trends are clear. $LiCoO_2$ is near-stoichiometric, whereas the nickel-containing samples are all lithium deficient and show significant enrichment in the nickel metal component.

Table 2
Estimated surface composition from AES and XPS data

| Bulk composition | Surface composition | |
|---|---|---|
| Compound | AES | XPS |
| $LiCoO_2$ | $Li_{1.09}Co_{1.08}O_2$ | $Li_{1.24}Co_{0.93}O_2$ |
| $LiNi_{0.5}Co_{0.5}O_2$ | $Li_{0.20}Ni_{1.13}Co_{0.88}O_2$ | $Li_{0.23}Ni_{1.03}Co_{0.85}O_2$ |
| Hexagonal $LiNiO_2$ | | |
| Synthesis I | $Li_{0.30}Ni_{1.53}O_2$ | $Li_{0.44}Ni_{1.31}O_2$ |
| Synthesis II | $Li_{0.42}Ni_{1.49}O_2$ | $Li_{0.55}Ni_{1.62}O_2$ |
| Cubic $LiNiO_2$ | $Li_{0.52}Ni_{1.39}O_2$ | $Li_{0.88}Ni_{1.27}O_2$ |

Perhaps surprisingly, the lithium depletion does not correlate with the lithium and transition metal ordering in forming the alternating Li/transition metal (1 1 1) planes as measured by the XRD I(0 0 3)/I(1 0 4) data, but rather with the final annealing temperature in the materials synthesis. The two synthesis protocols for producing hexagonal $LiNiO_2$ yielded I(0 0 3)/I(1 0 4) = 0.40 and 1.6 for synthesis I and II, respectively, indicating a much better ordering for samples produced by synthesis II. However, the lithium concentrations are only slightly higher for hexagonal $LiNiO_2$ II. The cubic $LiNiO_2$ material has a very small intensity of the (0 0 3) XRD diffraction feature, but has the highest concentration of surface lithium, depleted by only approximately 12–48%, depending upon whether AES or XPS analysis is used.

Auger data appear to indicate a lower lithium concentration than those obtained by XPS measurements. This is most likely a result of the different surface depths sampled by the two techniques. While cobalt, nickel and oxygen kinetic energies for the transitions chosen in AES and XPS for each of the elements are comparable, the lithium 1s and Auger KLL kinetic energies are substantially different, at approximately 1200 and 40 eV, respectively. The mean free path of the XPS 1s transition is substantially longer than that of the KLL AES transition, at about 5 and 12 Å, respectively [69]. Thus, the Auger data, which are more surface-sensitive to lithium, indicate that lithium depletion is greater in the near-surface area than do the XPS data, which samples further into the bulk material. The exception to this is the mixed transition metal compound $LiNi_{0.5}Co_{0.5}O_2$, for which the AES and XPS data indicate similar surface concentrations. These samples are severely delithiated, a condition that extends over the sampling depth of both AES and XPS techniques.

## 4. Discussion

The cobalt cation in $LiCoO_2$ is formally $Co^{3+}$, a particularly energetically favorable configuration in which the low-spin $d^6$ electrons populate a full $t_{2g}$ subshell. It is, therefore, not

surprising that $LiCoO_2$ presents a stable, well-behaved surface. The composition is approximately stoichiometric, the Co 2p binding energies and peak shapes are characteristic of the octahedrally-coordinated, diamagnetic $Co^{3+}$, and the lattice O 1s binding energy of 529.2 eV is not out of line with that of similar cobalt oxide materials. The surface can be contaminated with significant amounts of carbonate and hydroxyl adsorbates, and these species can be difficult to remove completely at temperatures that do not damage the surface, but this is not unexpected for air-exposed oxides.

The nickel-containing lithium metal oxides, however, are more problematic. Formally, nickel is $Ni^{3+}$ in stoichiometric $LiNiO_2$. However, an octahedrally-coordinated $Ni^{3+}$ presents a $d^7$cation that is not particularly stable in the solid state [70]. Two different descriptions of the nickel cation in $LiNiO_2$ have emerged in response to this. In one, the cation is assumed to be $Ni^{3+}$, a $d^7$ species that undergoes Jahn-Teller distortion [71], [72] and [73], somewhat ameliorating the poor stability of a $d^7$ octahedral cation. The lattice oxygen should formally remain $O^{2-}$ for this system, although depending upon the amount of the distortion, the charge-transfer overlap between Ni 3d and O 2p could be affected, which should manifest itself by a change in the Ni 2p satellite structure described by Eq. (1b). The second model creates a localized $Ni^{2+}$-$O^{1-}$ charge-transfer pair, producing a "NiO" like octahedral $Ni^{2+}$ and a relatively electron-poor lattice oxygen.

The picture that emerges here does not completely agree with either idealized model, but shows a near-surface area depleted in lithium and Ni 2p photoemission less sensitive to the nickel environment than has previously been assumed. The Ni 2p region is very similar to that observed for NiO, including the binding energies of the $2p_{3/2}$ and $2p_{1/2}$ transitions, satellite intensities and peak shapes. This is true for single crystal NiO, hexagonal $LiNiO_2$ with its Jahn-Teller distorted $Ni^{3+}$ cation, cubic $LiNiO_2$ which should have oxygen to nickel charge transfer closely related to the rocksalt NiO, and the mixed transition metal $LiNi_{0.5}Co_{0.5}O_2$ which has $Co^{3+}$ cations available to balance out the $Li^+$ near-surface concentration. All materials show remarkably similar Ni 2p photoemission. However, the O 1s XP spectrum yields an extremely low binding energy indicative of a very electron-rich lattice oxygen (528.4–528.7 eV) incompatible with a $Ni^{2+}$-$O^{1-}$ charge-transfer couple. The Ni 2p spectral region is complex and while the main $2p_{3/2}$ can be fit to at least two peaks, it closely reproduces the structure seen for well-characterized single crystal NiO substrates and thus characteristic of an octahedral $d^8$ cation. Due to uncertainties in the background removal and peak fitting process, structure due to small amounts of $Ni^{3+}$ ($\lesssim$10–15%) or other nickel species might be present in the Ni 2p region, but the spectrum is dominated by that obtained on octahedrally-coordinated $Ni^{2+}$, similar to that found in NiO.

To explain these results, we turn to studies on the lithium bulk deintercalation of hexagonal $LiNiO_2$, a process which is generally reversible down to concentrations of approximately $Li_{0.3}NiO_2$ [74]. The process is complicated by the tendency for nickel to substitute for lithium as $Ni^{2+}$ within the lithium $\langle 1\ 1\ 1 \rangle$ planes, which hinders the lithium mobility and creates nickel-excess nonstoichiometry within the bulk phase. The actual bulk stoichiometry should then formally be represented as $[Li_{1-x}Ni^{2+}{}_x]_{3a}[Ni^{3+}{}_{1-x}Ni^{2+}{}_x]_{3b}O_2$, where 3a and 3b represent the lithium and nickel sites, respectively, in an $R\bar{3}m$ structure. While originally described as rhombohedral throughout the process, recent studies [73] and [75] indicate that several ordered phases can take place as the substrate is delithiated. The majority of these are reported to involve ordering of lithium vacancies, and the generation of even higher nickel oxidation states. However, one structure observed on severely delithiated materials involves an alteration in stacking structure along $\langle 1\ 1\ 1 \rangle$ from O-Li-O-Ni-O, etc. of the ideal stoichiometric structure to include clustering of O-Ni units, that is O-Li-O-Ni-O-Ni-O-Li [74]. Thus, there is a natural tendency toward creation of a "NiO"-like environment for nickel cations even in the $LiNiO_2$ bulk.

The surface is not simply NiO however, as is indicated by the lithium and oxygen XPS data, both sets of which present unique 1s binding energy signatures. Thus, the surface is not merely phase-separating into $Li_2O$ and NiO, since neither lithium nor oxygen binding energies support lithium oxide formation. The charge-transfer band structure of the metal oxide (Eq. (1)) appears to carry over for adjacent lithium-oxygen ions, giving a relatively low binding energy for lithium due to the partially covalent nature of the bond. However, the process is not as efficient for the poorly-directed, and more highly ionic, Li 1s orbitals as for the 3d transition metal oxide, and the O 1s indicates a greater electron density on the oxygen when lithium is involved. The result of "lithium doping" is an extremely electron-rich oxygen.

The lattice oxygen is still able to hybridize effectively with the nickel 3d band, as indicated by the Ni 2p satellite structure which require that O 2p orbitals overlap with partially empty Ni $3d_{z2}$ and $3d_{x2-y2}$-derived band structure directed towards the neighboring oxygen atoms in the cubic structure. That this band has some $Ni^{3+}$ character is necessary to preserve charge neutrality in the near-surface region. The 2p satellite structure is characteristic of the nickel metal cation with partially unfilled $t_{2g}$ levels, but is not particularly sensitive to subtle differences in electron density or distortion of the octahedral environment around the nickel cation, since cubic and hexagonal $LiNiO_2$ both show comparable Ni 2p photoemission structure.

The conditions under which surface compositional analysis have been performed are, of course, significantly different than those encountered in the operation of lithium batteries. Near-surface concentrations of lithium may be substantially repopulated under electrochemical discharging conditions under which $Li^+$ migrate to and are re-incorporated into the $LiMO_2$ electrode. However, the present studies have several implications for elucidation of surface mechanisms and compositions of these materials. We have found no evidence for the existence of a $Ni^{2+}$-$O^-$ lattice couple but rather find an extremely electron-rich lattice oxygen. This is true for all nickel-containing lithium oxides studied here, regardless of degree of lithium depletion.

Also, adding cobalt to the $LiNiO_2$ lattice does not seem to make the surface any better behaved than that of the $LiNiO_2$

substrate. Rather, it appears harder to form a bulk solid solution of the mixed transition metal oxide $LiNi_{0.5}Co_{0.5}O_2$ and conditions necessary to promote a homogeneous, crystalline bulk may be too harsh to preserve the stoichiometry of the surface. TEM structural studies of the closely related material $LiNi_{0.8}Co_{0.2}O_2$ [25] find an approximately 5 nm thick surface region with substantial nickel and lithium disordering of the layered $R\bar{3}m$ bulk structure. Instead of stabilizing the substrate properties of nickel-containing lithium oxides to more closely resemble $LiCoO_2$, $LiNi_{0.5}Co_{0.5}O_2$ appears to be closer in surface oxygen and lithium chemical environment to $LiNiO_2$ as measured by XPS and to have inherited problems of lithium depletion of this material.

There are also implications for the usage of surface analysis in determining nickel oxidation state and chemical environment for these and related nickel oxide materials. Common practice of fitting complex, asymmetric Ni 2p XPS data to yield several different "states" should be performed only when substantial and obvious differences are found relative to spectra taken on single-component $3d^8$ NiO or other relevant reference compounds. Even then, results can be misleading, as can be seen by comparing the relatively simple 2p peak shape of $Co_3O_4$, which contains both octahedral $Co^{3+}$ and tetrahedral $Co^{2+}$, with the more complex CoO spectrum in which a single cobalt state is found as octahedrally coordinated $Co^{2+}$.

## 5. Conclusion

$LiCoO_2$, hexagonal $LiNiO_2$, cubic $LiNiO_2$, and the mixed transition metal oxide $LiNi_{0.5}Co_{0.5}O_2$ have been studied by Auger electron and X-ray photoelectron spectroscopies. $LiCoO_2$ has surface composition and cation environments that are easily inferred from those of the bulk. The surface of all nickel-containing metal oxides, however, has been found to be lithium-deficient and the nickel cation is comparable to "NiO" in its apparent chemical environment as measured by XPS. Even the more severely lithium depleted surfaces show a very electron-rich lattice oxide due to less efficient charge-transfer overlap between lithium and neighboring oxygen than is available with the nickel cation.

**Acknowledgements**

The authors gratefully acknowledge support by the National Science Foundation under Grant CHE-0213320 and the Nebraska Research Initiative.

## References

[1] W.A. van Schalkwijk and B. Scrosati, Advances in Lithium Ion Batteries, Kluwer Academic/Plenum Publishers, New York, N. Y. (2002).

[2] B. Scrosati, *Chem. Rec.* **5** (2005) (5), p. 286.

[3] A. Gotcher, *Adv. Mater. Process.* **163** (2005) (12), p. 32.

[4] E.S. Takeuchi, R.A. Leising, D.M. Spillman, R. Rubino, H. Gan, K.J. Takeuchi and A.C. Marschilok, *Lithium Batteries* (2004), p. 686.

[5] A.J. deButhune and N.A. Swendeman-Loud, Standard Aqueous Electrode Potentials and Temperature Coefficients at 25 °C, C.A. Hampel Pub. Co., Skokie, Ill (1964).

[6] B. Huang, Y.-I. Jang, Y.-M. Chiang and D.R. Sadoway, *J. Appl. Electrochem.* **28** (1998), p. 1365.

[7] K.M. Abraham, D.M. Pasquariello and E.M. Willstaedt, *J. Electronchem. Soc.* **145** (1998), p. 482.

[8] H. Abe, T. Murai and K. Zaghib, *J. Power Sources* **77** (1999), p. 110.

[9] W. Li, H.-P. Lin and D.L. Chua, *Proc. Power Source Conf.* **36** (1994), p. 254.

[10] G. Ceder, Y.-M. Chiang, D.R. Sadoway, M.K. Aydinol, Y.-I. Jang and B. Huang, *Nature* **392** (1998), p. 694.

[11] M. Contestabile, S. Panero and B. Scrosati, *J. Power Sources* **92** (2001), p. 65.

[12] M.D. Levi, K. Gamolsky, D. Aurbach, U. Heider and R. Oesten, *Electrochim. Acta* **45** (2000), p. 1781.

[13] G.X. Wang, J. Horvat, D.H. Bradhurst, H.J. Liu and S.X. Dou, *J. Power Sources* **85** (2000), p. 279.

[14] A.N. Mansour, J. McBreen and C.A. Melendres, *J. Electrochem. Soc.* **146** (1999), p. 2799.

[15] X. Li, F. Kang, W. Shen and X. Shi, *Key Eng. Mater.* **280–283** (2005), p. 443. |

[16] J. Cho and B. Park, *J. Power Sources* **92** (2001), p. 35.

[17] F. Ronci, B. Scrosati, V. Albertini and P. Perfetti, *J. Phys. Chem. B* **105** (2001), p. 754.

[18] C. Julien, *Solid State Ionics* **136/137** (2000), p. 887.

[19] H.J. Orman and P.J. Wiseman, *Acta Cryst. C* **40** (1984), p. 12.

[20] A. Hirano, R. Kanno, Y. Kawamoto, Y. Takeda, K. Yamaura, M. Takano, K. Ohyama, M. Ohashi and Y. Yamaguchi, *Solid State Ionics* **78** (1995), p. 123.

[21] J.B. Goodenough, D.C. Wickham and W.J. Croft, *J. Phys. Chem. Solids* **5** (1958), p. 107.

[22] W. Li, J.N. Reimers and J.R. Dahn, *Phys. Rev. B* **46** (1992), p. 3246.

[23] Y. Koyama, T. Mizoguchi, H. Ilkeno and I. Tanaka, *J. Phys. Chem. B* **109** (2005) (21), p. 10749.

[24] A. Rougier, C. Delmas and A.V. Chadwick, *Solid State Commun.* **94** (1995), p. 123.

[25] D.P. Abraham, R.D. Twesten, M. Balasubramanian, J. Kropf, D. Fischer, J. McBreen, I. Petrov and K. Amine, *J. Electrochem. Soc.* **150** (2003), p. A1450.

[26] J.-H. Chung, Th. Proffen, S. Shamoto, A.M. Ghorayeb, L. Croguennec, W. Tian, B.C. Sales, R. Jin, D. Mandrus and T. Egami, *Phys. Rev. B* **71** (2005) (6) 064410/1.

[27] F. Gendron, S. Castro-Garcia, E. Popova, S. Ziolkiewicz, F. Soulette and C. Julien, *Solid State Ionic* **157** (2003), p. 125.

[28] M.E. Arroyo y de Dompablo, A. Van der Ven and G. Ceder, *Phys. Rev. B* **66** (2002) 064112/1.

[29] P. Kuiper, G. Kriozomga, J. Ghijsen and G.A. Sawatzky, *Phys. Rev. Lett.* **62** (1989), p. 221.

[30] W.C. Mackrodt, N.M. Harrison, V.R. Saunders, N.L. Allan and M.D. Towler, *Chem. Phys. Lett.* **250** (1996), p. 66.

[31] L.A. Montoro, M. Abbate, E.C. Almeida and J.M. Rosolen, *Chem. Phys. Lett.* **309** (1999), p. 14.

[32] Y. Uchimoto, H. Sawada and T. Yao, *J. Power Sources* **97/98** (2001), p. 326.

[33] J.P. Kemp and P.A. Coc, *J. Phys. Condens. Matter* **2** (1990), p. 9653.

[34] A. Bannerjee, S.M. Chaudhari, D.M. Phase and B.A. Dasannacharaya, *Nucl. Instrum. Methods Phys. Res.* **199** (2003), p. 406.

[35] V. Bianchi, D. Caurant, N. Baffier, C. Belhomme, E. Chappel, G. Chouteau, S. Bach, J.P. Pereira-Ramos, A. Sulpice and P. Wilmann, *Solid State Ionics* **140** (2001), p. 1.

[36] A. Alcantara, P. Lavela, J.L. Tirado, R. Stoyanova, E. Kuzmanova and E. Zhecheva, *Chem. Mater.* **9** (1997), p. 2145.

[37] F. Sveg, B. Orel and V. Kaucic, *Solar Energy* **68** (2000), p. 523.

[38] K.-S. Park, S.-H. Park, Y.-K. Sun, K.-S. Nahm, Y.S. Lee and M. Yoshio, *J. Appl. Electrochem.* **32** (2002), p. 1229.

[39] C.-C. Chang, N. Scarr and P.N. Kumta, *Solid State Ionics* **112** (1998), p. 329.

[40] C. Julien, C. Letranchant, S. Rangan, M. Lemal, S. Ziolkkiewicz, S. Castro-Garcia, L. El-Farh and M. Benkaddour, *Mater. Sci. Eng. B* **76** (2000), p. 145.

[41] E. Levi, M.D. Levi, G. Salitra, D. Aurbach, R. Oesten, U. Heider and L. Heider, *Solid State Ionics* **126** (1999), p. 97.

[42] Z.H. Lu, X.J. Huang, H. Huang, L.Q. Chen and J. Schoonman, *Solid State Ionics* **120** (1999), p. 103.

[43] R. Kanno, H. Kubo, Y. Kawamoto, T. Kamiyama, F. Izumi, Y. Takeda and M. Taknao, *J. Solid State Chem.* **110** (1994), p. 216.

[44] J. McBreen, X.-Q. Yang, M. Balasubramanian and X. Sun, *Proc. Electrochem. Soc.* **36** (2001), p. 252.

[45] M.H. Nassir and M.A. Langell, *Solid State Commun.* **92** (1994), p. 791.

[46] G. Carson, M.H. Nassir and M.A. Langell, *J. Vac. Sci. Technol.* **A14** (1996), p. 1637.

[47] M.A. Langell, J.G. Kim, D.L. Pugmire and W. McCarroll, *J. Vac. Sci. Technol.* **19** (2001), p. 1977.

[48] A. Fujimori and F. Minami, *Phys. Rev. B* **30** (1984), p. 957.

[49] Z.X. Shen, J.W. Allen, P.A.P. Lindberg, D.S. Dessau, B.O. Wells, A. Borg, W. Ellis, J.S. Kang and S. Oh, *Phys. Rev. B* **42** (1990), p. 1817.

[50] A.N. Mansour, *Surf. Sci. Spectra* **3** (1996), p. 279.

[51] J. Stoch and J. Gablankowska-Kukucz, *Surf. Interface Anal.* **17** (1991), p. 165.

[52] D. Briggs and M.P. Seah, Practical Surface Analysis (second ed.), John Wiley & Sons, New York (1983) pp. 635–638.

[53] C.R. Brundle and H. Hopster, *Springer Ser. Chem. Phys.* **9** (1979), p. 272.

[54] J. van Elp, J.L. Wieland, H. Eskes, P. Kuiper, G.A. Sawatzky, F.M.F. de Groot and T.S. Turner, *Phys. Rev. B* **44** (1991), p. 6090.

[55] M.A. Langell, J.G. Kim, D.L. Pugmire and W. McCarroll, *J. Vac. Sci. Technol.* **19** (2001), p. 1977.

[56] M.A. Langell, G.A. Carson, M. Anderson, S. Smith and L. Peng, *Phys. Rev. B* **59** (1999), p. 4791.

[57] G. Carson, N.H. Nassir and M.A. Langell, *J. Vac. Sci. Technol.* **A14** (1996), p. 1637.

[58] S.A. Chambers, *Surf. Sci. Reports* **39** (2000), p. 105.

[59] M.A. Langell and M.H. Nassir, *J. Phys. Chem.* **99** (1995), p. 4162.

[60] M.A. Langell, C.L. Berrie, M.H. Nassir and K.W. Wulser, *Surf. Sci.* **320** (1994), p. 25.

[61] R. Domnick, G. Held, P. Witte and H.-P. Steinruck, *J. Chem. Phys.* **115** (2001), p. 1902.

[62] J.G. Kim, D.L. Pugmire, D. Battaglia and M.A. Langell, *Appl. Surface Sci.* **165** (2000), p. 70.

[63] M.W. Nydegger, G. Couderc and M.A. Langell, *Appl. Surface Sci.* **147** (1999), p. 58.

[64] L. Tan and W.C. Crone, *Acta Mater.* **50** (2002), p. 4449.

[65] J.-K. Kang and S.-W. Rhee, *Thin Solid Films* **391** (2001), p. 57.

[66] A. Davidson, J.F. Tempere, M. Che, H. Roulet and G. Dufour, *J. Phys. Chem.* **100** (1996), p. 4919.

[67] K.S. Kim and N. Winograd, *Surf. Sci.* **43** (1974), p. 625.

[68] A.F. Carley, S.D. Jackson, J.N. O'Shea and M.W. Roberts, *Surf. Sci.* **440** (1999), p. L868.

[69] A. Zangwill, Physics at Surfaces, Cambridge University Press, New York (1988) p. 21.

[70] F.A. Cotton and G. Wilkenson, Advanced Inorganic Chemistry (fifth ed.), Wiley-Interscience (1998).

[71] A. Rougier and C. Delmas, *Solid State Commun.* **94** (1995), p. 123.

[72] R.R. Urbano, A. Garcia, E. Granado, J.A. Sanjurjo, I. Torriani, C. Rettori, S.B. Oseroff, A. Hassan, G.B. Martins, Z. Fisk, P.G. Pagliuso, J.L. Sarrao, R. Caciuffo and R.M. Ibberson, *Phys. Rev. B: Condens. Matter Mater. Phys.* **64** (2000), p. 9593.

[73] M.E. Arroyo y de Dompablo, A. Van der Ven and G. Ceder, *Phys. Rev. B* **66** (2002), p. 064112.

[74] T. Ohzuku, A. Ueda and M. Nagayama, *J. Electrochem. Soc.* **140** (1993), p. 1862.

[75] L. Croguennec, C. Pouillerie and C. Delmas, *J. Electrochem. Soc.* **147** (2000), p. 1314.